Shedding Light on the Birth of Hybrid Perovskites: A Correlative Study by In Situ Electron Microscopy and Synchrotron-Based X-ray Scattering

Charles Sidhoum, Doru Constantin, Dris Ihiawakrim, Marc Lenertz, Thomas Bizien, Clément Sanchez, Ovidiu Ersen

Shedding light on the birth of hybrid perovskites: a correlative study by *In-Situ* electron microscopy and synchrotron-based X-rays scattering

Charles Sidhoum[1], Doru Constantin[2], Dris Ihiawakrim[1], Marc Lenertz[1], Thomas Bizien[3], Clément Sanchez[4,5] and Ovidiu Ersen[1,*]

[1] *Institut de Physique et Chimie des Matériaux de Strasbourg, CNRS and Université de Strasbourg, 23 rue Lœss, 67034 Strasbourg, France*

[2] *Institut Charles Sadron, CNRS and Université de Strasbourg, 23 rue Lœss 67034 Strasbourg, France*

[3] *Synchrotron SOLEIL, L'Orme des Merisiers, 91 192 Saint-Aubin, Gif-sur-Yvette, France*

[4] *USIAS, University of Strasbourg Institute for Advanced Study, 5 Allée du Général Rouvillois, F-67083 Strasbourg, France*

[5] *Laboratoire de Chimie de Matière Condensé de Paris, Sorbonne Université, 4 Place Jussieu, 75005 Paris, France*

Abstract

Lead halide perovskites have emerged as promising candidates for a broad range of optoelectronic devices thanks to their unique physical properties. Methylammonium lead iodide (MAPI) perovskite has been the most commonly studied LHPs due to its very promising optoelectronic properties. One of the main explored pathways for obtaining MAPI perovskite is the synthesis by Ligand-Assisted Reprecipitation (LARP); however, this method is not totally understood from a phenomenological point of view. In this study, we took advantage of the development of a series of advanced *in-situ* techniques to bring new insight into the pathway of this process that leads to MAPI perovskite from a precursor solution. First, we monitored the nucleation and the growth processes of a solvated-intermediate phase obtained by LARP by correlating local information obtained by a direct visualization of the reaction medium using liquid-phase Transmission Electron Microscopy (TEM), and more global information brought by synchrotron-based X-ray scattering measurements. This combined analysis, in real time and in representative conditions of the synthesis method, allowed us to decipher the structural evolution of the emerging phases, from amorphous and roughly spherical objects in the early stages of the process toward elongated ribbon-like morphology particles after a few seconds, through a crystallization process. Secondly, we followed *in-situ* the transition of the as-obtained solvated-intermediate phase towards the final phase of MAPI perovskite during a thermal treatment at 80°C, using in this case a combination of gas-phase TEM, in image and diffraction modes, and temperature-resolved X-Ray diffraction We provided direct and unprecedented evidence of the fragmentation of the crystals, simultaneously to the occurrence of the

structural transformation between the intermediate and final phases. Our approach, that involved also challenging development of new correlative methods, demonstrates the high interest of such *in-situ* correlative study for a better understanding of the synthesis and properties of new emerging materials such as LHPs.

Introduction

Lead halide perovskites (LHPs) of general formula APbX3 (A: monovalent cation; X: halogen) is one of the most studied classes of perovskites due to their great versatility[1] and broad range of application in optoelectronic devices such as photodetectors[2], light-emitting diodes[3], lasers[4,5] and solar energy conversion[6,7]. About fifteen years ago, Kojima et al. reported the development of LHPs as visible-light sensitizers in solar cells with a power conversion efficiency (PCE) of 3.8%[8]. Meanwhile, the research on perovskite solar cells has shown remarkable progress, pushing the limits farther ahead and allowing to reach a recent certified PCE record of 25.6%[9] in 2022, value which can be even superior to 33% with the design of tandem perovskite/silicon-based solar cell[10]. The classical methylammonium lead iodide perovskite, $CH_3NH_3PbI_3$ (MAPI), is the most used compound considered systematically in these materials [11]. There is a broad range of synthesis pathways to obtain MAPI nanocrystals (NCs) or more generally LHP NCs including hot injection[12–14], mecanosynthesis[15–18], vapor-assisted solution deposition[19], Ligand-Assisted Reprecipitation (LARP)[20–22], and many others[23–25]. The first attempt to synthesize LPHs by LARP approach was reported by Papavassiliou et al.[26] in 2012 with the synthesis of $CsPbBr_3$ NCs. In 2014, Pérez-Prieto et al.[20] used a similar approach to synthesize organic-inorganic LHP $CH_3NH_3PbBr_3$ which has been subsequently adapted to many varieties of hybrid LHP NCs[27–30]. Note that the LARP synthesis method is a simple and versatile technique, done at room temperature with the use of low-cost solvents such as toluene, N,N-dimethylformamide (DMF), dimethylsulfoxide (DMSO), acetonitrile, octadecene etc. The crystallization occurs by simple mixing of two solvents with different polarities (i.e., polar and apolar) in the presence of ligands[31]. DMF and DMSO are the two widely used polar solvents to dissolve the precursors prior to mixing with the apolar solvent[32]. However, it has been shown that these two coordinating solvents lead to the formation of solvated intermediates, which require annealing to obtain the optoelectronically interesting hybrid LHPs phase[33–35]. Nevertheless, the pathway of formation of hybrid LHP NCs via solvated intermediates promotes the quality of the crystallization[36]. In particular, focusing on the DMF intermediates in MAPI synthesis, Petrov et al.[37] reported that depending on the ratio of precursor in the mixing solution, different compositions of intermediate phase can be obtained and have a strong impact on the crystallinity of the final product. Using a different ratio of DMSO and DMF in the precursor solution, Ren et al.[38] showed that a good control on the stoichiometry of the intermediate phase dramatically influences the crystallization of perovskite films and enhances efficient perovskite solar cells. Munir et al.[39] highlighted the importance of the precursor solvate phases and the impact of the halide composition on the latter to guide the final photovoltaic performance.

Despite the amount of work carried out to optimize the optoelectronic properties of these promising materials, there is a clear lack of comprehension of the phenomena at the origin of LHPs crystallization, especially when the above-mentioned intermediate phases are involved in the formation process. It is generally admitted that new insight into the crystallization pathway of these materials, including a complete visualization at different

scales of the evolution of the process, is one of the current challenges in the perovskite community. In this context, the recent advances in the development of new *in-situ* transmission electron microscopy (TEM) approaches allow now visualizing phenomena at the nanoscale in their native environment, whether gaseous or liquid[40] (GP-TEM or LP-TEM for respectively Gas Phase-TEM or Liquid Phase-TEM). The possibility to use these techniques as *in-situ* characterisation tools is now considered a major step forward for monitoring, with high spatial resolution, chemical and physical phenomena using TEM. A wide range of processes can be now directly visualized using *in-situ* TEM, to cite a few: biomineralization of calcium carbonate[41], morphological evolution of catalysts during electrochemical reaction[42,43], nucleation and growth of particles[44–46] etc. Regarding the perovskite field and the thousands of works published on this topic each year, only a handful reported the use of this tool, and their focus is mainly on monitoring the degradation of the material exposed to different factors such as moisture, light, and electron beam radiation[47–54]. To the best of our knowledge, to date only two articles focused on the growth of LHPs NCs using *in-situ* TEM as main tool: Wang et al.[55] studied the growth dynamic of MAPI films with the influence of urea in the precursor solution, whereas Qin et al.[56] reported the first observations of nucleation and growth of MAPI NCs using electron-beam assisted solvent evaporation approach. Nevertheless, any consistent *in-situ* TEM study should report on the direct observation of nucleation and growth process, in the synthesis media, of LHP NCs or their intermediate phase obtained by LARP. The absence of such a study can be explained, at least in part, by the difficulty of reproducing the real experimental synthesis conditions, by minimizing the influence of the electron beam, in the LP-TEM cell[57,58] combined with the beam-sensitive nature of hybrid perovskite which makes difficult even the classical TEM analysis[59].

In this study, we present a first insight into the nucleation and growth of an intermediate phase derived from MAPI at the nanoscale by using a combined characterization approach that includes LP-TEM and synchrotron-based X-Rays scattering experiments. Our goal is to determine the process onset and kinetics, as well as to obtain direct information on the evolution of the system during the different steps of the process, as for instance the occurrence of possible intermediate phases. Once the presence of such intermediate phases is demonstrated, we investigate the phase transition towards MAPI perovskite during an annealing step by combining GP-TEM, temperature-resolved X-Ray diffraction (XRD) and thermogravimetric analysis (TGA). The combination of these very complementary techniques is decisive for providing a comprehensive description of this last step in the formation of MAPI perovskite.

Materials and Methods

LARP synthesis approach

The chemicals were purchased from Sigma-Aldrich and used as received. The LARP protocol was first developed based on the literature[28–30,60] and then adapted to the observations and the various tests carried out. The whole synthesis is performed in ambient atmosphere. In a typical synthesis, 0.2mmol of PbI_2 (Lead (II) iodide, ≥99% anhydrous) and 0.16mmol of CH_3NH_3I (Methylammonium iodide, ≥99% anhydrous) were dissolved separately in DMF (N,N – Dimethylformamide anhydrous, 99.8%, SigmaAldrich) and then mixed with the addition of 0.5mL of oleic acid (Oleic acid, technical grade, 90%) and 40µL of octylamine (Octylamine, 99%). Then 20µL of the precursor mixture was dropped into 2mL of toluene (Toluene anhydrous, 99.8%, SigmaAldrich) and instant precipitation of a white colloid was observed (Figure S. 1). The solution was centrifugated at 8000rpm during 5min, the supernatant was discarded and the as-obtained precipitate is redispersed in toluene for further characterizations. The $CH_3NH_3PbI_3$ black phase is obtained by annealing the white precipitate at 80°C for 4 hours in an oven in ambient atmosphere.

In-situ TEM

LP-TEM

The direct monitoring of the nucleation and growth processes of the intermediate phase under electron beam is obtained using a flow liquid cell (Protochips Inc., Raleigh, NC, USA) with a 150nm liquid spacing bottom E-chip (EPB-55DNF-10, Protochips Inc., Raleigh, NC, USA; see Figure 2.A) closed with a top E-chip (EPT-55DW-10, Protochips Inc., Raleigh, NC, USA). The holder (Fusion Select, Protochips Inc., Raleigh, NC, USA) is directly introduced in a corrected JEOL 2100F/Cs TEM, placed into a vacuum column, and imaged at 200kV. The cell is first filled with toluene using one inlet with a 50µL/min flow rate, the injection is stopped when toluene starts to come out of the outlet. Then the precursor mixture in DMF is injected using a low flow rate (1µL/min) by the second inlet (see Figure S. 2). Data was collected using the Protochips AXON *in-situ* TEM software.

GP-TEM

The direct recording of the phase transition from the intermediate phase to the MAPI perovskite phase under electron beam is obtained using a flow-heating liquid cell (Protochips Inc., Raleigh, NC, USA) with a 500nm spacing. The use of heating liquid cell is more adapted to low temperatures compared to gas cells which present a significative temperature gradient below 100°C. To reproduce the laboratory conditions, ambient air is injected (10µL/min) using one of the two inlets of the sample holder. A small drop (1µL) of the intermediate phase solution in suspension in toluene is deposited and dried on the bottom E-chip (EPB-55GF-10, Protochips Inc., Raleigh, NC, USA). The system is closed using a large top E-chip (EHT-45ZZ-10, Protochips Inc., Raleigh, NC, USA) and then heated using Protochips AXON Poseidon software from 25°C to 80°C with a step of 1°C/min. Data were collected using the Protochips AXON *in-situ* TEM software.

Ex-situ TEM characterization

Ex-situ classical high-resolution TEM (HR-TEM) and electron diffraction of the different phases were carried out in a LaB6 TEM operating at 200kV. The samples were deposited on a holey carbon-coated TEM grid. Chemical analysis using Energy-Dispersive X-Ray Spectroscopy (EDXS) was performed on samples *ex-situ*. *In-situ* chemical analysis is not relevant because of the abundance of Pb and I in solution.

X-Ray Diffraction

The XRD measurements were carried out on a D8 Discover diffractometer in Bragg Brentano geometry equipped with a Cu Sealed tube ($\lambda_{K\alpha1}$ = 1.54059 Å), a quartz front monochromator, a motorized anti-scatter screen, and an energy-resolved Lynxeye XE-T linear detector. The XRD temperature-dependent measurements were carried out using the same diffractometer without the anti-scatter screen and equipped with an Anton Paar TTK600 Temperature chamber. Each measurement has been taken at a constant temperature and a heating rate of 10°/min was applied in between the measurement. A diffraction pattern is acquired every 10°C from 30°C to 100°C and every 25°C from 100°C to 300°C. The measurements were carried out at atmospheric pressure in ambient atmosphere.

A Rietveld refinement of the XRD experimental spectra was performed by using the Fullprof software[61] with the Thompson-Cox-Hastings pseudo-Voigt convoluted with axial divergence asymmetry peak function and the March function for preferential orientation[62]. The experimental data were fitted with a limited number of parameters: lattice parameters, linear interpolation between 4 background points, a scale factor for each phase, the crystallite size parameters and a preferential orientation parameter. Structure used are the one reported in the ICDD PDF files for MAPI and PbI_2 respectively PDF n°01-085-5508 and n°00-007-0235; the structure used for the PbI_2-rich intermediate phase are the one reported by Petrov et al.[37]. The references structures were not refined.

Time-resolved *in-situ* SAXS/WAXS

The SAXS/WAXS experiments were performed on the SWING beamline of the synchrotron SOLEIL with a photon energy of 12keV and a sample-to-detector (Dectris EigerX 4M) distance of 6.48m for SAXS and 0.783m for WAXS measurements, leading to the following q-ranges: $0.001 \leq q\ (Å^{-1}) \leq 0.16$ and $0.01 \leq q\ (Å^{-1}) \leq 1.24$ for the SAXS and WAXS configurations, respectively.

LARP synthesis was reproduced using a “stop-flow” device (SFM-4000 apparatus from BioLogic) which allows the fast injection (dead time <5ms) of the mixture directly in the capillary. A description of the entire procedure followed for using the stop-flow system is given in the Supplementary Information.

Results and Discussion

The intermediate phase and its structural characteristics

In the first part, we synthesized the MAPI-derived intermediate phase using LARP method. This phase was subsequently thoroughly characterized *ex-situ* using TEM and XRD. We then studied the pathway of nucleation and growth to obtain the same product *in-situ* through a combination of LP-TEM, for providing a direct visualization of the synthesis medium at the nanoscale and synchrotron-based X-ray scattering, in order to acquire correlated real time bulk information.

Ex-situ characterization of the intermediate phase

The observation of a white precipitate as a final product following the LARP synthesis is initially reported. This precipitate was identified as the orthorhombic *Pnnm* PbI_2-rich intermediate phase with the general formula 2MAI-3PbI_2-2DMF (MA = $CH_3NH_3^*$), already reported in the literature[35,37,63]. The identification of the PbI_2-rich intermediate phase was made by comparing the XRD pattern obtained (Figure 1.A) with the one reported by *Petrov et al.*[37] The occurrence of the PbI_2-rich phase is consistent with the molar ratio used during the LARP synthesis, with an excess precursor of PbI_2 compared to MAI (see Materials and Methods). We observed low angle diffraction peaks (6.5°, 8° and 9.5°) typical of the PbI_2-rich intermediate structure with longer interplanar distances of the intermediate phase due to intercalation of both DMF and MA^+ molecules in between layered PbI_6 octahedra (Figure 1.B).

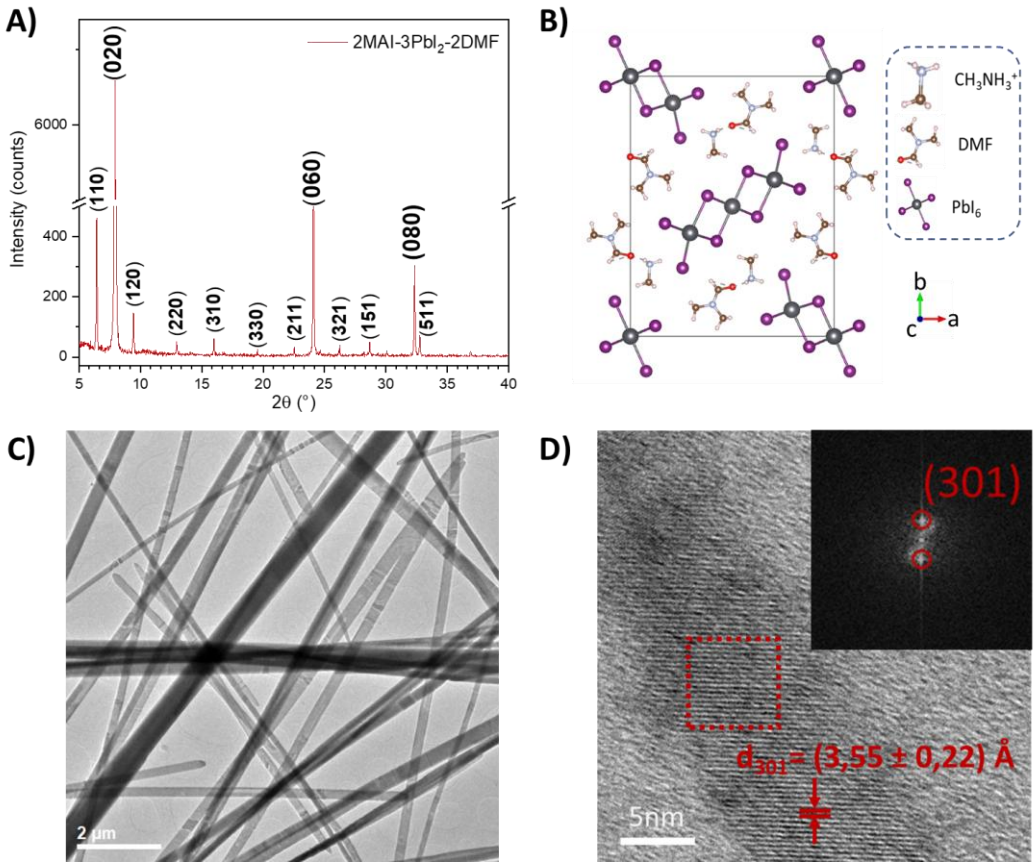

Figure 1: A) Diffraction pattern of the identified 2MAI-3PbI$_2$-2DMF intermediate phase; B) Crystallographic structure of the PbI2-rich intermediate phase, obtained from Crystallographic Information File (CIF) provided by Petrov et al.[37]; C) TEM image of the crystal of 2MAI-3PbI$_2$-2DMF phase. D) HR-TEM image of monocrystalline object with FFT (insert) of the region of interest (red dotted square). Identification of the (301) plan (red circles on the FFT); the red arrows indicate the d-spacing of the (301) plan on the HR-TEM image.

Conventional TEM was then carried out to characterize the morphology and the chemical composition of the final product. The synthesized crystals have an anisotropic elongated ribbon-like shape (Figure 1.C) as expected, given the crystal structure of the intermediate phase[34]. They exhibit significant width polydispersity (Figure S. 4) with an average width ± SD of 230 ± 115nm, highlighting the difficulty of obtaining a narrow size distribution using the LARP approach. The length of the crystals varies from a few µm to a few tens of µm. For a reliable structural assignment, we performed an in-depth analysis of the experimental XRD data using a Rietveld refinement (Figure S. 3.A). Firstly, this analysis confirmed the presence of the PbI_2-rich phase from the structure provided by Petrov et al.[37] Secondly, it revealed a significant preferential orientation along the [0k0] direction, while the [00l] peaks were nearly absent. Despite the [0k0] preferential orientation makes no doubt, the [110] peak was slightly under-evaluated in this model. The March parameter was found to be 0.19[62], clearly bellow 1. This is generally the characteristic of plate-like crystallites and not of needle-likes. However, this is compatible with a ribbon-like structure with the [0k0] direction aligned along the ribbon's length, explaining why those plans are unlike to diffract, and the [h00] direction oriented parallel to the ribbon's width. The treatment of the preferential orientation by the March function favour (or disadvantage) one direction and makes no difference between other directions (at the same azimuth from the first one). This works well for needle of plates but with ribbon's like crystallites the probability of orientation is no more equivalent for all directions at a same azimuth from the preferential orientation direction. This is why the under-evaluation of the [110] peak notably in the fitted data (Figure S. 3.A) support our ribbon-like shape hypothesis.

The presence of the (301) type plane in the FFT of the high-resolution TEM image acquired on a small typical monocrystalline object (Figure 1.D), having an interatomic distance of (3.55 ± 0.22) Å, confirms our findings. This value is consistent with that obtained for the intermediate phase by Petrov et al.[37], further validating the ribbon-like structure. Additionally, the observed contrast difference in the superposition of the crystals, characteristic of a thin sample, provides further evidence supporting the elongated ribbon-like structure. However, to maintain consistency with the existing literature, we will continue to use the term "needle" in this paper, as in addition it is commonly associated to strongly anisotropic intermediate phase crystals[34,36,37]. Nevertheless, accordingly to our results, we admit that these crystals are more likely flattened needles, resembling to ribbons as regarding their structure and morphology. From the chemical point of view, elemental mapping (Figure S. 5) using energy-dispersive X-ray spectroscopy (EDXS) was carried out, confirming the homogeneous composition of Pb and I in the crystals.

Real-time visualization of the nucleation of 2MAI-3PbI$_2$-2DMF

To explore the crystallization of 2MAI-3PbI$_2$-2DMF phase by LP-TEM, we used the LP-TEM cell configuration schematized in Figure 2. A. The cell is composed of two silicon chips with overlapping electron transparent silicon nitride (SiN_x) membranes. A syringe pump system

allows us to first fill the LP-TEM cell with toluene and then to inject the precursor mixture, in DMF, which will lead to the precipitation observable at the level of the SiN_x membrane. The experimental protocol to reproduce the synthesis conditions with the LP-TEM sample holder is detailed in Supplementary Information (Figure S. 2). The electron beam irradiation may have an important influence on the chemical evolution of the system[64–66], especially in a liquid media[67–69]. To mitigate the electron beam effect, we performed our experiments at a very low dose rate ($0.1e^-/A^2s$). *Wang et al.*[55] showed that an electron flux of $0.1e^-/A^2s$ does not lead to any side effect from the electron beam on the growth process of MAPI perovskite in an LP-TEM cell. Nevertheless, comparison with unexposed areas is mandatory to ensure the negligible contribution of the beam to our observations.

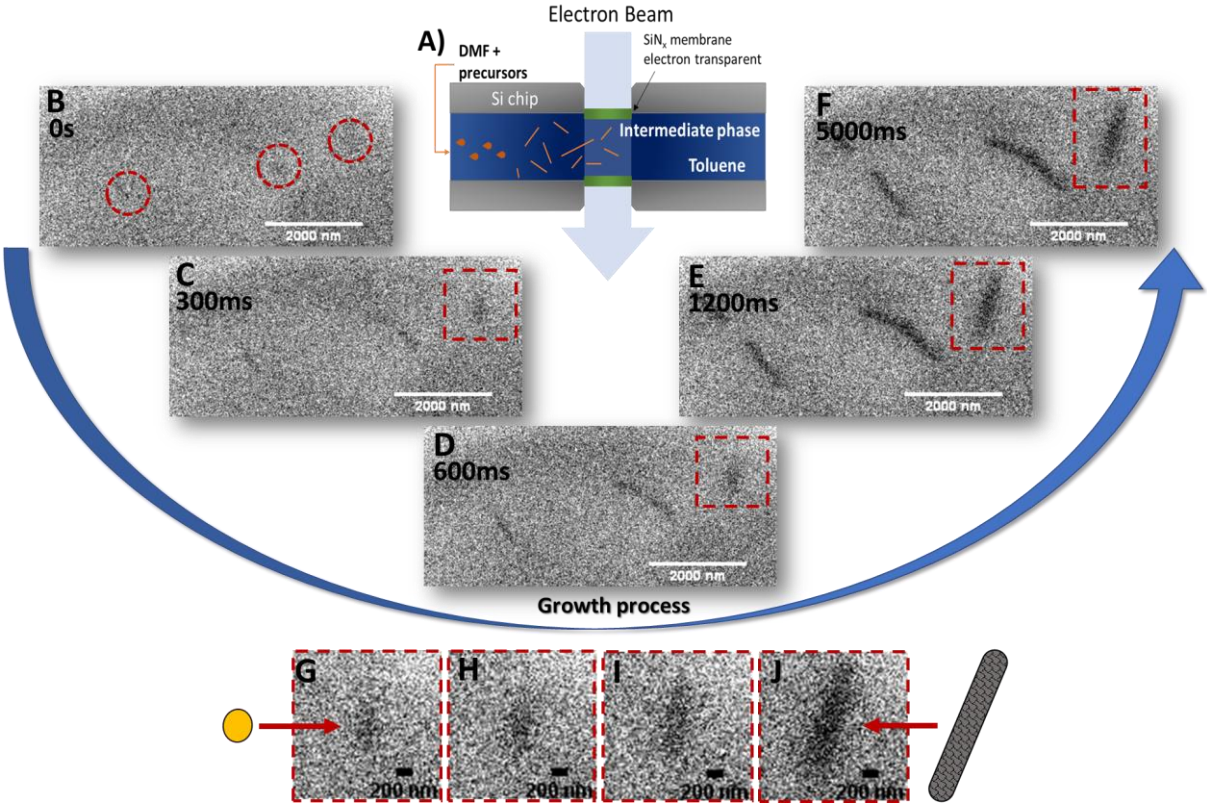

Figure 2: A) Scheme of the liquid cell used for in-situ LP-TEM experiment; B-F) Sequences from the chronological evolution of the nucleation and growth processes of the 2MAI-3PbI$_2$-2DMF phase by LP-TEM. The red circles indicate the sites of nucleation at t_0;G-J) Magnified images, respectively of images C to F, of the growth of a single particle. The area considered are delimited by red dotted squares in images C to F. ; the yellow sphere and grey needle schematized the morphology adopted by the system. Images are filtered using ImageJ software.

Figure 2. B-F) displays some typical *in-situ* TEM images extracted from the direct monitoring of the nucleation and growth of the intermediate phase (see also Movie S.1). The process occurred in 5 seconds following a time scale of the crystallization process similar to that reported in the literature from other studies and characterization techniques[70,71]. To the best of our knowledge, this is the first direct visualization at the nanoscale of the nucleation and growth of a hybrid perovskite-derived crystal reported in the literature. Areas unexposed to the electron beam were also imaged (Figure S. 6.A-C; Movie S.2), demonstrating that the crystallization is not induced by the electron beam. Statistical analysis of the sizes (Figure S. 6.D) of these needle-like crystals allows the estimation of an

average width of 91 ± 29nm, whereas the length varies from a few hundred nm to about 1µm. This difference in size observed between *ex-situ* and *in-situ* measurements is explained by the confinement intrinsic to the cell used for the LP-TEM experiment, which shortens the growth step shorter and reduces the final size of the objects compared to the bulk experiments.

A closer look at a single particle (Figure 2. G-F) monitored during the process provides direct information on its morphologic evolution. The particle is roughly ellipsoidal during the first seconds of growth (Figure 2. G-I)) but adopts an anisotropic shape at the end of the crystallization (Figure 2. J)). We can estimate the evolution of the length and the width of the crystal during the growth process (summarized in Figure S. 7) showing considerable increase of the length compared to the width, as expected for the growth of an anisotropic object.

Correlative analysis of the LP-TEM and *in-situ* SAXS/WAXS data

In addition to the localized information obtained from LP-TEM, to obtain ensemble averaged and more representative information, in particular regarding the kinetics, we combined the LP-TEM results with *in-situ* SAXS and WAXS data. The protocol for reproducing the LARP synthesis using a stopped-flow device, the data acquisition, and a description of the data processing of the SAXS/WAXS raw data, are given in SI.

By following the above-mentioned protocol, we first studied the crystallization of the system using WAXS. Figure S. 8 shows a typical WAXS pattern obtained during the first available moment after the introduction of the mixing solution (precursor mixture in DMF and toluene with a 1:5 ratio, as described in SI). The plot of the scattered intensity as a function of the modulus of the scattering vector q (I=f(q)) features three strong Bragg peaks at q = 0.46 $Å^{-1}$, 0.57 $Å^{-1}$ and 0.67 $Å^{-1}$. The latter is typical of the intermediate phase 2MAI-3PbI_2-2DMF[72,73]. It is worth noticing that these peaks were already identified as belonging to the stoichiometric intermediate MAI-PbI_2-DMF structure[74,75]. Distinguishing the exact structure is challenging due to the small variation (up to 0.03 $Å^{-1}$) of the peaks in the low q region (q < 0.8 $Å^{-1}$) attributed to a different amount of DMF incorporated among the lamellar plane of edge-sharing PbI_6 octahedron in the intermediate structure (Figure 1.B). Nevertheless, our experimental configuration setup (resolution in q range up to 0.01 $Å^{-1}$) allows us to obtain a clear distinction between these two possible intermediate phases[37,72] and to conclude in our case as to the occurrence of the PbI_2-rich 2MAI-3PbI_2-2DMF phase[72], in agreement with the previous identification by XRD (Figure 1.A). Besides, we noticed the lack of peak at q = 0.9 $Å^{-1}$ and 1 $Å^{-1}$ characteristic respectively of PbI_2 and tetragonal MAPI perovskite phase, indicating a good correlation with the lab bench synthesis mentioned above (Figure 1.A). Moreover, from Figure S. 8 we can deduce that the crystallization occurs after 750ms, as shown by the appearance of the peak at q = 0.47 $Å^{-1}$. This is a clear indication that, during the nucleation and growth process observed in LP-TEM experiments (as schematized in Figure 2 and 3) the crystalline phase is already formed. However, we can also hypothesize the existence of an amorphous phase in the earlier stages of the process (t<750ms).

In a second step of the analysis, we analysed the evolution of the scattering signal in a SAXS configuration after the introduction of the mixing solution.

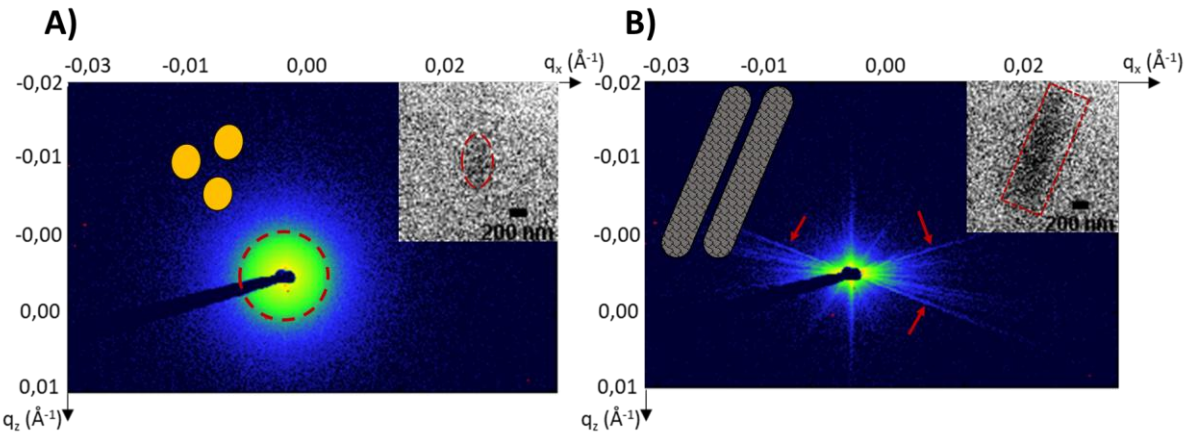

Figure 3: SAXS images acquired at: A) first detectable image after the injection (considered as t_0); B) t_0+5850ms. The dotted red circle indicates the isotropic scattering signal; the red arrows indicate the anisotropic scattering signal. TEM images extracted at t+300ms and t +5000ms from LP-TEM experiments, inserted to illustrate the morphology adopted by the system at these specific times. A schematic view of the morphology adopted by the objects is added to the figure (yellow circles and grey needles)

Figure 3 presents the SAXS images obtained at two characteristic times (t_0 and t_0+5850ms), similar to the times assigned to the beginning and to the end of the growth process deduced from the LP-TEM experiment. We noticed the appearance of an isotropic signal on the first image we could acquire after the precursor injection (dotted red circle in Figure 3.A), as well as the predominance of an anisotropic signal (red arrows in Figure 3.B) after about 6s. Both observations are coherent with the morphology observed at similar times in the LP-TEM, as illustrated by the TEM images shown in insert in Figure 3. The complete evolution of the signal is shown in Figure S. 9 and indicates the decrease of the previously mentioned isotropic signal concomitantly with the emergence of the anisotropic signal. These first observations lead us to perform a specific data processing, which consists of the separation of the two types of signals (i.e., anisotropic and isotropic) by applying different masks on the SAXS scattering patterns. First, the total signal is obtained by simply applying a mask on the beam stop and the dead zones of the detector (Figure S. 15. A). Then, the isotropic signal, which does not present angular dependence, is obtained by applying a mask on a specific area which does not contain the anisotropic signal (Figure S. 15. B). The anisotropic signal is obtained from the subtraction of the isotropic signal from the total signal. A complete description of the separation of the signal and the data processing is given in the Supplementary information. Figure 4 shows the isotropic and total scattered intensity as a function of the modulus of q, at different times. Superposition between the isotropic signal (dotted lines) and the total signal (solid lines) is observed during the first moments (from 0s to 600ms) after reactant mixing, consistent with the observations of the scattering SAXS patterns. A deviation between these two signals becomes clear at 2400ms and increases progressively with time (at 4500ms and 5850ms).

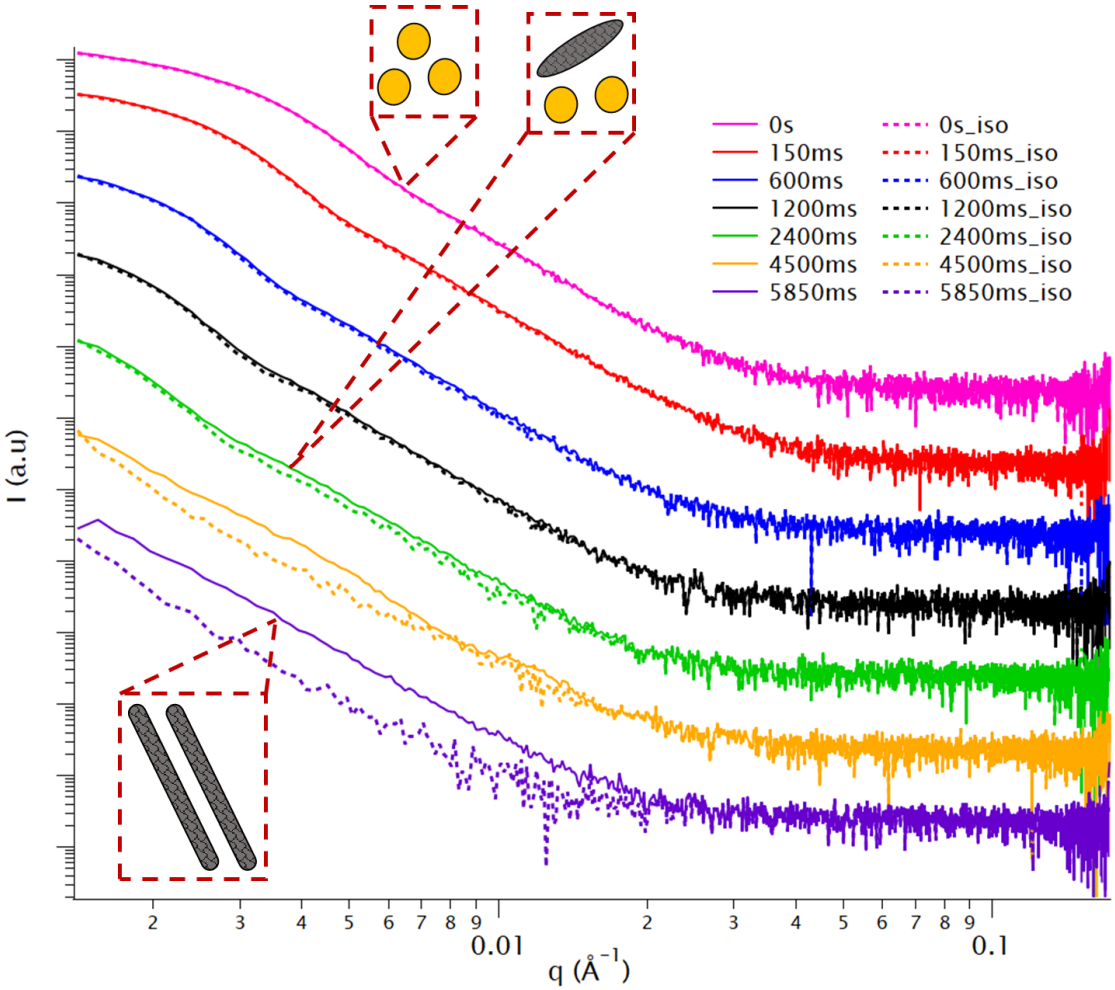

Figure 4: SAXS curves, at different times, of the scattered intensity as a function of the modulus of q vector, obtained after a data processing step of the images shown in Figure S. 9. Solid lines correspond to the total signal, dotted lines correspond to the isotropic signal (see SI for more details). The inserts (red dotted squares) schematize the morphology of the objects at different times.

We have fitted the isotropic signal with a Schulz distribution of polydisperse spheres (see Supplementary information for more details on the fit procedure). A typical example of the fitting procedure on the first curve after the injection (i.e. t_0) is shown in Figure S. 16.A (corresponding to the dotted pink line in Figure 4). The complete set of the fitted curves is shown in Figure S. 17. The experimental curves and the model are in very good agreement during the very first moments after the injection (t<2400ms), without any significant discrepancy between the experimental data and the model. Beyond 2400 ms, when the total signal starts to separate from the isotropic signal, the model is no longer in agreement with the experimental data, suggesting that the objects are no longer spherical and begin to adopt the anisotropic shape of the intermediate phase. We could also extract from the fit the mean diameter of the spheres at different times, as shown in Figure S 16.B. This geometrical parameter increases from 100nm to more than 250nm, value which corresponds to the very first ellipsoidal objects observed in the LPTEM experiment (Figure 2. G-I). We could also estimate from the fits the evolution of the volume fraction (Figure S. 16.C), which decreases continuously. This tendency confirms the transformation of the spheres into the needle-like crystals characteristic of the intermediate phase. The polydispersity shows no significant variation (Figure S. 16.D).

We hypothesize that during the first moment after mixing the two solvents, the reaction medium leads to the aggregation of the precursor monomers due to the strong change of polarity of the predominant solvent (apolar toluene) leading to the nucleation and growth of amorphous spheres. This assumption is supported by the WAXS data, which do not present a crystalline peak at the early stages of the process. For t<2400ms, these spheres increase progressively in size with time, as shown by the evolution of the mean diameter extracted from the fit of the isotropic curves (Figure S. 16.B). This mechanism can be consistent with the visualization of the ellipsoidal objects in the LP-TEM experiments. For t>2400ms, the size of the particles became too large in order to be visualized by our TEM set up, but the deviation between the isotropic signal and the total signal provides direct evidence of the fact that the system evolves toward anisotropic objects, as observed in Figure 2. J and Figure 3.B.

The subtraction of the isotropic signal from the total signal allowed us to estimate the anisotropic component (see SI), which is plotted in Figure S. 9. For t>2000ms, this anisotropic signal follows a q^{-4} law (black dotted line in Figure S. 10), compatible with the existence of large objects with typical dimensions out of the q range of the experimental setup. It can be assumed that these objects are the anisotropic needle-like crystals similar to those obtained by the classical LARP protocol and observed in the *ex-situ* analysis (Figure 1. C-D) as well as during the LP-TEM experiments (Figure 2 and Figure S. 6.A-C). The WAXS measurements (Figure S. 8) for t>750ms indicate that these objects crystallize into the PbI_2-rich 2MAI-3PbI_2-2DMF phase, which also supports the previous argument.

Direct insight into the transformation of the intermediate phase in $CH_3NH_3PbI_3$

To remove the solvated DMF (Figure 1. B) and subsequently obtain the optoelectronically interesting black phase[76,77] of MAPI perovskite ($CH_3NH_3PbI_3$), it is well known that an annealing step between 80 and 100°C allows to obtain the final phase[78–82]. First information was obtained by analysing *ex-situ* by TEM and XRD a dried precipitate of the intermediate 2MAI-3PbI_2-2DMF annealed in an oven in ambient atmosphere at 80°C for four hours.

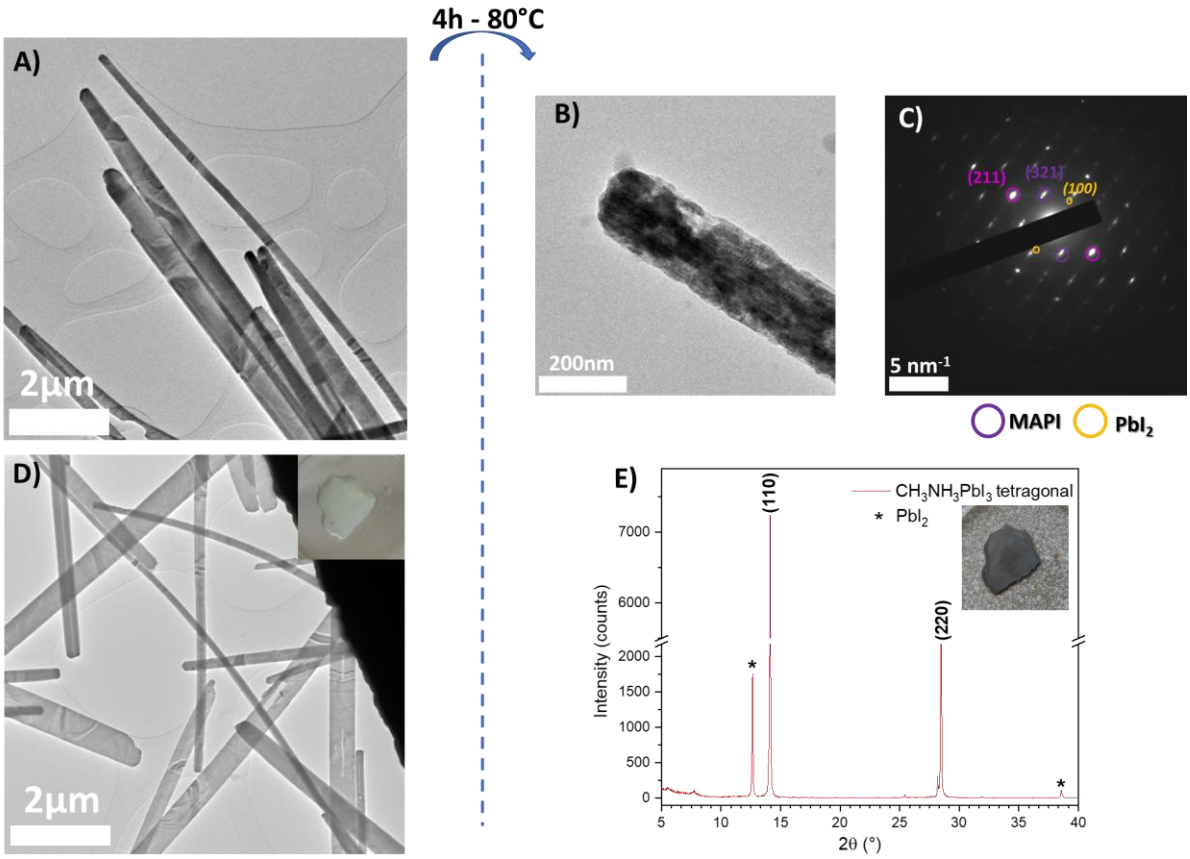

Figure 5: A, D) Typical TEM image of the initial anisotropic crystals; insert on D: photo of the white precipitate of the intermediate phase. B) TEM images of the samples after 4h of annealing at 80°C. C) Electron diffraction pattern of the nanorod shown in image B – purples circles are characteristics of the MAPI phase (ICDD n°01-085-5508), whereas yellow circles indicate the presence of PbI_2 hexagonal phase (ICDD n°00-007-0235). E) Diffraction pattern of the MAPI tetragonal phase (ICDD n°01-085-5508) obtained after annealing; insert: photo of the black precipitate of MAPI phase obtained after annealing.

The characteristics of the initial PbI_2-rich intermediate phase, in particular its needle-like morphology and specific crystallinity, were confirmed by TEM and XRD analyses carried out before the annealing step (Figure 5. A, D and Figure 1. A). The morphological assignment made in the first part of the work, as regarding the ribbon-like morphology of the crystals, is supported by the thin aspect of the crystals observed in Figure 5. D. After annealing, a significant morphological change occurs, consisting in the fragmentation of the crystals into smaller crystals (Figure 5.B). A similar structural aspect has already been reported for MAPI nanowires in the literature[83]. The formation of tetragonal *I4cm* MAPI was demonstrated by XRD (Figure 5. E) which highlighted its high crystallinity[84,85]. In particular, the XRD pattern shows the presence of two characteristic *hkl* plans (110) and (220) respectively at 14.1° and 28.4°, concomitantly with the appearance of a peak at 12.6° identified as the (001) plan of the PbI_2 hexagonal phase. This indicates that the well-known thermal degradation[33,86] of MAPI into PbI_2 is already initiated during the annealing. The strong preferential orientation, along the [110] direction, for the deposited samples[87] is confirmed by a Rietveld refinement of the diffractogram (Figure S. 3.B). This refinement enabled a precise indexation of both phases (i.e. MAPI and PbI_2). Similar to what was observed in the refinement of the intermediate phase (Figure S. 3.A), the XRD spectra of the two phases are affected by a

preferential orientation respectively, for MAPI and PbI_2, along [110] and [001]. Specifically, MAPI demonstrates a preferential orientation along [110], consistent with a plate-like morphology similar to the smaller crystals obtained after annealing (Figure 5. B). This substantial change in morphology will be discussed in detail later. The electron diffraction pattern (Figure 5.C) are also in good agreement with the XRD analysis. We identified both the tetragonal phase of MAPI and the PbI_2 hexagonal phase thanks to the presence of the (211) and (321) plan for MAPI and (100) for PbI_2. As shown in the photos inserted in Figure 5. D, E, we also observed an obvious colour change of the precipitate, from white to black, as expected for the final MAPI black phase.

Real-time monitoring of the phase transition, in the real space, by GP-TEM

We carried out GP-TEM experiments to obtain direct monitoring of the phase transition under electron beam. To mimic the conditions of the phase transition studied *ex-situ* (Figure 5), ambient air from the room was injected into the TEM sample holder and the temperature was set at 80°C. Figure 6 displays a sequence of *in-situ* TEM images extracted from the direct recording (Figure 6. A-D) and their respective electron diffraction patterns (Figure 6. E-H) acquired during the annealing of the sample at 80°C. At 25°C, as expected, the well-defined anisotropic morphology of the PbI_2-rich intermediate phase and its crystalline network[36] can be, once again, clearly evidenced (Figure 6.A-E). The complete transformation into tetragonal MAPI perovskite is already achieved after 45min of annealing at 80°C, as shown by the indexation of the MAPI crystalline phase (Figure 6.F). As already assumed from the *ex-situ* data, the needle fragments into smaller crystals by preserving the anisotropic framework. We also observed the presence of the (002) plan of PbI_2, consistent with the transition observed *ex-situ* (Figure 5.C, E). During the time, the MAPI crystalline phase is globally preserved (Figure 6. G-H) but the crystals start to be damaged jointly to the appearance of small particles around the needle. These damages are probably due to the repeated exposure to electron beam during the electron diffraction acquisition. Figure S. 18 shows another region of interest monitored during the annealing of the sample. Similar observations can be made, in particular the direct visualization of the structural transition from the intermediate phase (Figure S. 18. E) toward MAPI tetragonal phase and PbI_2 (Figure S. 18.F-H), as well as the fragmentation of the well-defined needle (Figure S. 18.A) into smaller crystals (Figure S. 18.B-D) and the precipitation of small particles. A closer look to the images of precipitated particles (Figure S. 19. A-B), completed by the analysis of the associated electron diffraction patterns (Figure S. 19.C) allows us to assign the particles to the PbI_2 phase, a general trend commonly observed during the exposure of perovskites to electron beam which induces their partial degradation. [87,88]. To confirm this assumption, we have also studied some unexposed area after the 4 hours of annealing in the E-TEM cell (Figure S. 20). We have observed similar morphological changes (Figure S. 20.A-C) and the presence of the same final phases (i.e. MAPI tetragonal phase and PbI_2) as identified by electron diffraction (Figure S. 20.D). We have noticed the absence of precipitated PbI_2 particles, demonstrates thus that its presence is the result of the decomposition of the MAPI crystals under electron beam originating from a persistent electron exposure during the acquisition of multiple diffraction patterns. Thus, there are two types of PbI_2: the nanoparticles as a by-product of decomposition under electron beam and the PbI_2 due to the annealing and the phase transition as already highlighted by the XRD analysis (Figure 5.E). Nevertheless, the textural change, as well as the phase transition, are the consequences of annealing.

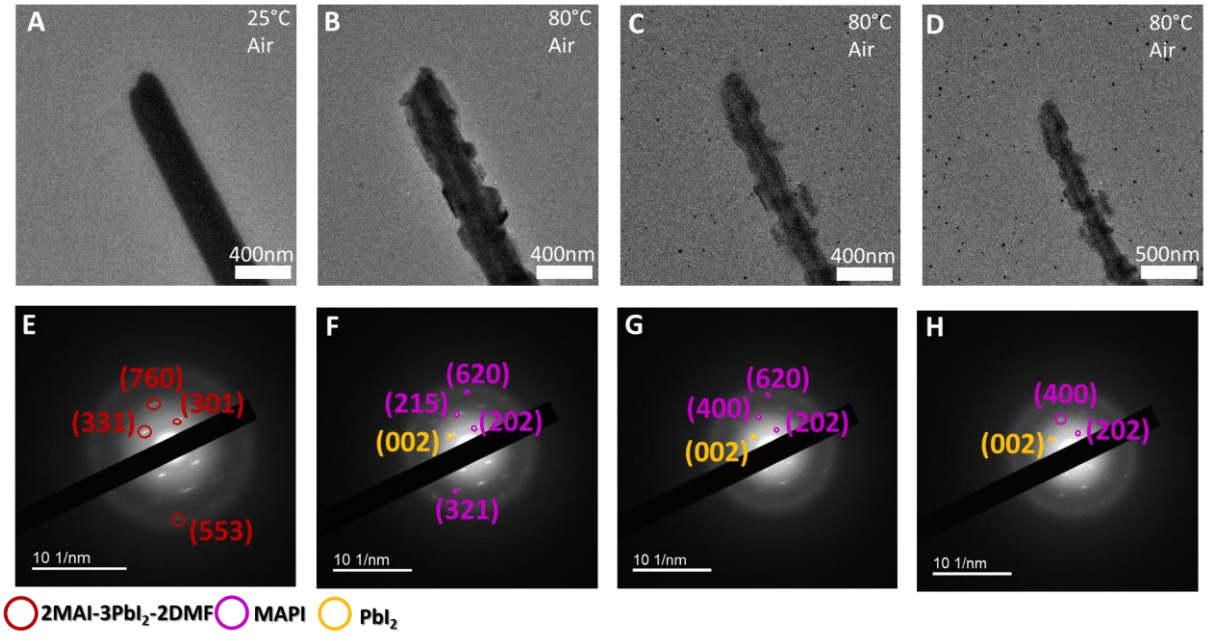

Figure 6 A-D) Sequence of in-situ TEM images of the crystals during annealing in the GP-TEM cell in ambient atmosphere (A: before annealing; B: 45min at 80°C; C: 2h30 at 80°C; D: 4h30 at 80°C). E-H) Electron diffraction patterns acquired on the areas shown in the TEM images, with the structural assignment (red circles: 2MAI-3PbI2-2DMF intermediate phase[36]; pink circles: MAPI perovskite tetragonal phase (ICDD n°01-085-5508); yellow circles: PbI_2 phase (ICDD n°00-007-0235)).

Structural evolution by temperature resolved XRD

In order to support the GP-TEM study, the phase transition previously observed by studied *ex-situ* and *in-situ TEM* was also monitored by temperature resolved XRD, in order to more precisely determine the different structural modifications undergoing during the process. The applied temperature protocol is described in Figure S. 21. Figure 7 shows the evolution of the diffraction pattern during the annealing process. We noted the stability of the PbI_2-rich intermediate phase until 70°C (XX domain in Figure 7), the temperature at which the characteristic peaks disappear abruptly. Concomitantly to the loss of the intermediate phase, we noted the rise in intensity of the (110) and (220) peaks from the MAPI tetragonal phase, similar to the *ex-situ* data, starting at ~ 50°C. This perovskite phase is predominant from 70°C to 170°C (XY domain in Figure 7) along with the emergence of the (001) peak of PbI_2 as previously observed (Figure 5. E). The thermal degradation of MAPI into PbI_2 continues until 300°C (YY domain in Figure 7) with a total and partial disappearance of the (110) and (220) peaks respectively, in the benefit of the increase in the intensity of the (001) characteristics PbI_2 peak. These results are in very good agreement with the structural behaviour deduced from the GP-TEM experiment. At 80°C the transition from 2MAI-3PbI2-2DMF phase to the MAPI phase is already complete, as observed during the GP-TEM experiment. The *in-situ* XRD experiment confirmed also the coexistence of the PbI_2 hexagonal phase with the MAPI phase once the structural transition is initiated, with corresponding *hkl* order in the XRD pattern ((001) in domain XY in Figure 7) and in the electron diffraction pattern (002) in Figure 6.F-H). Finally, we were able to correlate these results with those obtained by TGA (Figure S. 22) in particular the very good agreement in the as-deduced characteristics temperatures. By TGA, a first weight loss from ambient

temperature to 95°C correspond to the loss of solvated DMF, a second transition is observed with the loss of MAI corresponding to the degradation of the MAPI tetragonal phase toward PbI_2; at the end, the last weight loss, observed for T>250°C, is assigned to the decomposition of PbI_2.

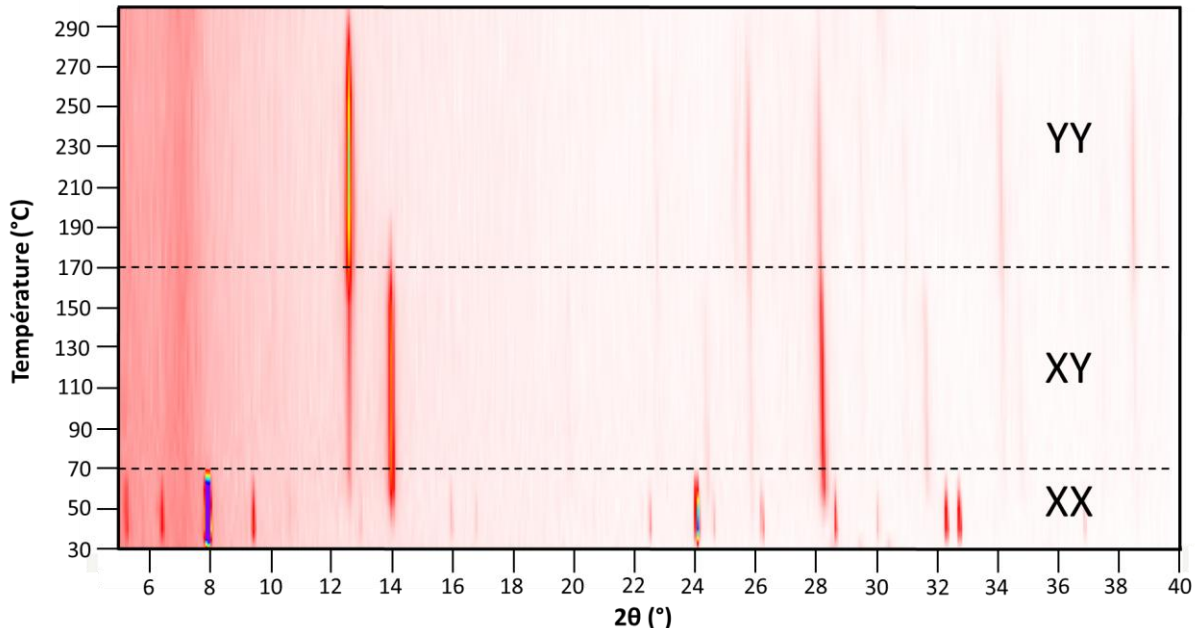

Figure 7: Temperature resolved X-ray 2D diffraction pattern of the annealing of the intermediate phase sample from 30°C to 300°C. Dotted lines and notation allow the distinction between the different phase regimes obtained during the annealing and are solely a guide for the eye. XX: intermediate phase 2MAI-3PbI2-2DMF; XY: MAPI perovskite phase (ICDD n°01-085-5508); YY: PbI_2 hexagonal phase (ICDD n°00-007-0235).

As illustrated by TEM, the structural transition from the 2MAI-3PbI2-2DMF intermediate phase to the tetragonal MAPI perovskite goes along with a dramatic change in the morphology of the crystals. Although atomic-resolution data during the in situ TEM monitoring is missing, we can use the benefit of a direct visualization of the morphological change of the crystals and the XRD Rietveld refinement findings (Figure S. 3. A-B), for understanding why the structural transition impacts the final morphology. The LARP approach can be described as a "chimie-douce" synthesis pathway, due to its soft conditions of work, in particular ambient temperature, atmospheric pressure and atmosphere medium. As described previously, these conditions may lead to the formation of a metastable phase, in particular the DMF-solvated 2MAI-3PbI2-2DMF intermediate phase. This phase undergoes a transition toward the thermodynamically stable phase, the tetragonal MAPI one, through annealing. The TGA analysis (Figure S.22), combined with the GP-TEM (Figure 6) monitoring and temperature-resolved XRD (Figure 7), indicates that the transition occurred simultaneously with the departure of the solvated DMF.

The crystalline structure of the intermediate phase (Figure 1. B) exhibits a non-continuous crystalline network, at the atomic level, and the Rietveld refinement (Figure S. 3.A) illustrates a preferential orientation along the [0k0] direction. Thus, this phase can be associated to a molecular crystal, in which the mobility of atoms is very important, an argument also supported by the ionic nature of such crystals[89]. In such a crystal, the departure of the DMF may induce important atomic mobility and a subsequent restructuration of the crystalline lattice, leading thus to a possible change in morphology. By

annealing, all the DMF molecules are lost while the MAI is retained, at least partly, as already reported by Gu et al.[35] As described before, our findings strongly suggest that the intermediate phase is made of ribbon-like crystallites or flattened needles. Starting from such a morphology, we can reasonably assume that, during the annealing, the ribbon-like crystals fracture into smaller crystals with a plate-like morphology. The fragmentation process seems to be in a good agreement with the sequential images obtained by GP-TEM. Furthermore, such a morphological change agrees also with the main result obtained by the refinement of the MAPI diffractogram (Figure S. 3.B) which shows a strong preferential orientation along the [110] direction. For both phases, plate-like preferential orientations are thus present, as demonstrated by the Rietveld refinement.

Conclusion

A consistent correlative study of the formation of the tetragonal MAPI phase by using the LARP approach followed by an annealing step was performed by combining *ex-situ* and *in-situ* techniques. The as-obtained multiple information regarding the formation process and the time evolution of the involved phases is schematized in Figure 8. Firstly, by mixing precursor mixture in DMF with a large volume of toluene, we revealed the presence of a PbI_2-rich intermediate phase, which was fully characterized by conventional TEM and XRD. The pathway of the nucleation and growth processes of this intermediate phase was explored in detail by a combination of LP-TEM and synchrotron-based SAXS/WAXS. The challenge for reproducing, in the liquid media, the processes in two different *in-situ* setups was achieved allowing to reach in both cases a sufficient time resolution in order to provide unprecedented structural information. The results obtained by the two techniques are in good agreement and highlight the appearance, at a very short time (of the order of few hundred ms), of amorphous roughly spherical objects which quickly crystallize into the 2MAI-3PbI_2-2DMF phase and grow to finally adopt the characteristic anisotropic needle-like shape of the DMF-solvate intermediate phase after few seconds. To the best of our knowledge, it is the first time that the formation of a hybrid halide perovskite-derived structure was observed *in-situ* by using a correlative approach combining real space and reciprocal space information.

In the second part of the work, in order to obtain direct insight on the second step of the whole synthesis protocol leading to the optoelectronically interesting MAPI tetragonal phase, we focused on assessing the structural evolution of the intermediate phase during annealing at 80°C. The tetragonal MAPI perovskite was firstly characterized *ex-situ*, in the final state, and then the transition from the intermediate phase was monitored directly by combining GP-TEM with temperature-resolved XRD and ATG measurements. This transition is very probably, at the origin of the fragmentation process of the ribbon/needle-like crystals present in the intermediate phase into smaller plate-like crystals characteristics of the tetragonal MAPI phase, in agreement with the electron diffraction data. The as-observed morphological transformation is supported also by the results obtained from a Rietveld refinement of the XRD data, which clearly indicated a plate-like preferential orientation in both the intermediate phase and the tetragonal MAPI phase obtained after annealing. These conclusions were supported by the XRD and ATG data and, altogether, allowed us to infer that the structural transition occurred concomitantly with the disappearance of the intermediate phase, starting from 50°C, with the release of the DMF solvated molecules and appearance of PbI_2 hexagonal phase.

This methodology can be transposed to the *in-situ* study of the formation and evolution of other solvated phases which depend on the molar ratio between the precursor or the use of DMSO to replace DMF. Studying all these different phases and their influence on the activation conditions and kinetics of the nucleation and growth processes involved in the formation of the intermediate phase and of the final MAPI perovskite will provide comprehensive insight into the global mechanism. Thorough understanding of these phenomena is essential to gaining better control of the final properties of these very promising materials. We believe that this work will serve as a reference, by allowing to transpose our findings to other LHP materials and associated processes, due to its advantage of providing deep understanding of the crystallization pathway.

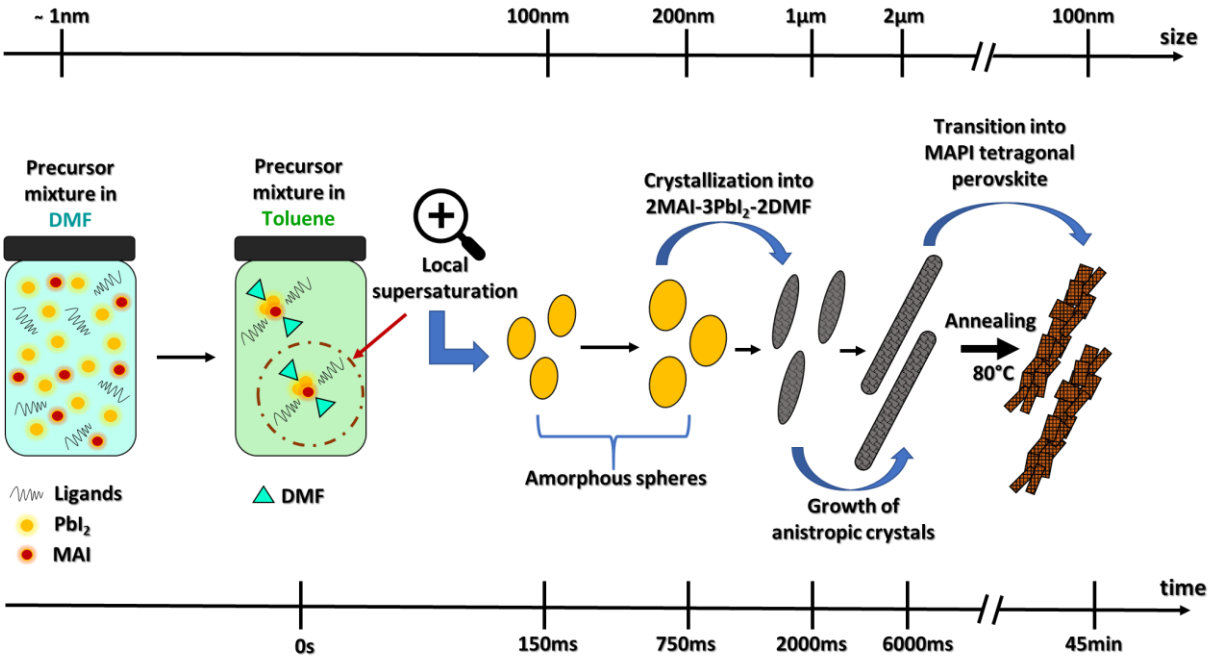

Figure 8: Schematic representation of the full process allowing to obtain the MAPI tetragonal perovskite from precursor solution following the LARP precipitation method and an additional annealing step.

Acknowledgements

This work of the Interdisciplinary Thematic Institute QMat, as part of the ITI 2021 2028 program of the University of Strasbourg, CNRS and Inserm, was supported by IdEx Unistra (ANR 10 IDEX 0002), and by SFRI STRAT'US project (ANR 20 SFRI 0012) and EUR QMAT ANR-17-EURE-0024 under the framework of the French Investments for the Future Program. This work was also supported by the USIAS chair of Prof. Clément Sanchez. The authors would like to thank D. Burger for the TGA measurements at IPCMS; SOLEIL for provision of synchrotron radiation facilities and Javier Perez for assistance in using beamline SWING; the beamline ODE at SOLEIL for the stopped-flow device; Dr. Nivedita Sudheer, Dr. Sharmin Sharna and Dr. Vinavadini Ramnarain for the assistance during the synchrotron session at SOLEIL.

ASSOCIATED CONTENT

Supplementary information

The following files are available free of charge (https://doi/xx.xx.xxxx/acscmxxxxxxx):

Figures S1, S2: scheme of the LARP synthesis method and the protocol used to reproduce it in the LPTEM cell. Figure S3: Rietveld refinement of the XRD data. Figures S4, S5, S6, S7, S8, S9, S10: additional characterization carried out for the study of the growth process of the intermediate phase. Figures S11, S12, S13: protocol employed for the use of the stopped-flow mixing system. Figures S14, S15, S16, S17, Table 1 and 2: SAXS/WAXS data acquisition, processing and fitting. Figures S18, S19 and S20: additional GP-TEM data. Figure S21: temperature ramp for the temperature-resolved XRD experiment. Figure S22: TGA experiment. (PDF file)

Movie S1: In situ TEM monitoring of the nucleation and the growth processes of the intermediate phase. (AVI file)

Movie S2: Direct observation of the intermediate phase in the LP-TEM cell. (AVI file)

Corresponding author

Pr. Ovidiu Ersen. *Institut de Physique et Chimie des Matériaux de Strasbourg, CNRS and Université de Strasbourg, 23 rue Lœss, 67034 Strasbourg, France*
E-mail : ovidiu.ersen@ipcms.unistra.fr
orci.org/0000-0002-1553-0915

Author Contributions

The manuscript was written through contributions of all authors. All authors have given approval to the final version of the manuscript.

Notes

The authors declare no competing financial interest.

References

(1) Gao, P.; Bin Mohd Yusoff, A. R.; Nazeeruddin, M. K. Dimensionality Engineering of Hybrid Halide Perovskite Light Absorbers. *Nature Communications 2018 9:1* **2018**, *9* (1), 1–14. https://doi.org/10.1038/s41467-018-07382-9.

(2) Wang, H.; Kim, D. H. Perovskite-Based Photodetectors: Materials and Devices. *Chem Soc Rev* **2017**, *46* (17), 5204–5236. https://doi.org/10.1039/C6CS00896H.

(3) Adjokatse, S.; Fang, H. H.; Loi, M. A. Broadly Tunable Metal Halide Perovskites for Solid-State Light-Emission Applications. *Materials Today* **2017**, *20* (8), 413–424. https://doi.org/10.1016/J.MATTOD.2017.03.021.

(4) Xing, G.; Mathews, N.; Lim, S. S.; Yantara, N.; Liu, X.; Sabba, D.; Grätzel, M.; Mhaisalkar, S.; Sum, T. C. Low-Temperature Solution-Processed Wavelength-Tunable Perovskites for Lasing. *Nat Mater* **2014**, *13* (5), 476–480. https://doi.org/10.1038/NMAT3911.

(5) Stranks, S. D.; Snaith, H. J. Metal-Halide Perovskites for Photovoltaic and Light-Emitting Devices. *Nature Nanotechnology 2015 10:5* **2015**, *10* (5), 391–402. https://doi.org/10.1038/nnano.2015.90.

(6) Correa-Baena, J.-P.; Saliba, M.; Buonassisi, T.; Grätzel, M.; Abate, A.; Tress, W.; Hagfeldt, A. Promises and Challenges of Perovskite Solar Cells. *Science (1979)* **2017**, *358* (6364), 739–744. https://doi.org/10.1126/science.aam6323.

(7) Grätzel, M. The Light and Shade of Perovskite Solar Cells. *Nature Materials 2014 13:9* **2014**, *13* (9), 838–842. https://doi.org/10.1038/nmat4065.

(8) Kojima, A.; Teshima, K.; Shirai, Y.; Miyasaka, T. Organometal Halide Perovskites as Visible-Light Sensitizers for Photovoltaic Cells. *J Am Chem Soc* **2009**, *131* (17), 6050–6051. https://doi.org/10.1021/ja809598r.

(9) Zhao, Y.; Ma, F.; Qu, Z.; Yu, S.; Shen, T.; Deng, H.-X.; Chu, X.; Peng, X.; Yuan, Y.; Zhang, X.; You, J. Inactive (PbI 2)2RbCl Stabilizes Perovskite Films for Efficient Solar Cells. *Science (1979)* **2022**, *377* (6605), 531–534. https://doi.org/10.1126/science.abp8873.

(10) *Best Research-Cell Efficiency Chart | Photovoltaic Research | NREL*. https://www.nrel.gov/pv/cell-efficiency.html (accessed 2023-02-15).

(11) Djurišić, A. B.; Liu, F. Z.; Tam, H. W.; Wong, M. K.; Ng, A.; Surya, C.; Chen, W.; He, Z. B. Perovskite Solar Cells - An Overview of Critical Issues. *Prog Quantum Electron* **2017**, *53*, 1–37. https://doi.org/10.1016/J.PQUANTELEC.2017.05.002.

(12) Akkerman, Q. A.; Park, S.; Radicchi, E.; Nunzi, F.; Mosconi, E.; de Angelis, F.; Brescia, R.; Rastogi, P.; Prato, M.; Manna, L. Nearly Monodisperse Insulator Cs4PbX6 (X = Cl, Br, I) Nanocrystals, Their Mixed Halide Compositions, and Their Transformation into CsPbX3 Nanocrystals. *Nano Lett* **2017**, *17* (3), 1924–1930. https://doi.org/10.1021/ACS.NANOLETT.6B05262/ASSET/IMAGES/LARGE/NL-2016-052624_0005.JPEG.

(13) Protesescu, L.; Yakunin, S.; Bodnarchuk, M. I.; Krieg, F.; Caputo, R.; Hendon, C. H.; Yang, R. X.; Walsh, A.; Kovalenko, M. v. Nanocrystals of Cesium Lead Halide

Perovskites (CsPbX3, X = Cl, Br, and I): Novel Optoelectronic Materials Showing Bright Emission with Wide Color Gamut. *Nano Lett* **2015**, *15* (6), 3692–3696. https://doi.org/10.1021/NL5048779/SUPPL_FILE/NL5048779_SI_001.PDF.

(14) Vybornyi, O.; Yakunin, S.; Kovalenko, M. v. Polar-Solvent-Free Colloidal Synthesis of Highly Luminescent Alkylammonium Lead Halide Perovskite Nanocrystals. *Nanoscale* **2016**, *8* (12), 6278–6283. https://doi.org/10.1039/c5nr06890h.

(15) Saski, M.; Prochowicz, D.; Marynowski, W.; Lewiński, J. Mechanosynthesis, Optical, and Morphological Properties of MA, FA, Cs-SnX3 (X = I, Br) and Phase-Pure Mixed-Halide MASnIxBr3–x Perovskites. *Eur J Inorg Chem* **2019**, *2019* (22), 2680–2684. https://doi.org/10.1002/EJIC.201801506.

(16) Zhu, Z. Y.; Yang, Q. Q.; Gao, L. F.; Zhang, L.; Shi, A. Y.; Sun, C. L.; Wang, Q.; Zhang, H. L. Solvent-Free Mechanosynthesis of Composition-Tunable Cesium Lead Halide Perovskite Quantum Dots. *Journal of Physical Chemistry Letters* **2017**, *8* (7), 1610–1614. https://doi.org/10.1021/ACS.JPCLETT.7B00431/SUPPL_FILE/JZ7B00431_SI_001.PDF.

(17) Protesescu, L.; Yakunin, S.; Nazarenko, O.; Dirin, D. N.; Kovalenko, M. v. Low-Cost Synthesis of Highly Luminescent Colloidal Lead Halide Perovskite Nanocrystals by Wet Ball Milling. *ACS Appl Nano Mater* **2018**, *1* (3), 1300–1308. https://doi.org/10.1021/ACSANM.8B00038/ASSET/IMAGES/MEDIUM/AN-2018-000384_M001.GIF.

(18) Yun, S.; Kirakosyan, A.; Yoon, S. G.; Choi, J. Scalable Synthesis of Exfoliated Organometal Halide Perovskite Nanocrystals by Ligand-Assisted Ball Milling. *ACS Sustain Chem Eng* **2018**, *6* (3), 3733–3738. https://doi.org/10.1021/acssuschemeng.7b04092.

(19) Sedighi, R.; Tajabadi, F.; Shahbazi, S.; Gholipour, S.; Taghavinia, N. Mixed-Halide CH3NH3PbI3−xXx (X=Cl, Br, I) Perovskites: Vapor-Assisted Solution Deposition and Application as Solar Cell Absorbers. *ChemPhysChem* **2016**, *17* (15), 2382–2388. https://doi.org/10.1002/CPHC.201600230.

(20) Schmidt, L. C.; Pertegás, A.; González-Carrero, S.; Malinkiewicz, O.; Agouram, S.; Mínguez Espallargas, G.; Bolink, H. J.; Galian, R. E.; Pérez-Prieto, J. Nontemplate Synthesis of CH3NH3PbBr3 Perovskite Nanoparticles. *J Am Chem Soc* **2014**, *136* (3), 850–853. https://doi.org/10.1021/ja4109209.

(21) Sun, S.; Yuan, D.; Xu, Y.; Wang, A.; Deng, Z. Ligand-Mediated Synthesis of Shape-Controlled Cesium Lead Halide Perovskite Nanocrystals via Reprecipitation Process at Room Temperature. *ACS Nano* **2016**, *10* (3), 3648–3657. https://doi.org/10.1021/acsnano.5b08193.

(22) Huang, H.; Xue, Q.; Chen, B.; Xiong, Y.; Schneider, J.; Zhi, C.; Zhong, H.; Rogach, A. L. Top-Down Fabrication of Stable Methylammonium Lead Halide Perovskite Nanocrystals by Employing a Mixture of Ligands as Coordinating Solvents. *Angewandte Chemie* **2017**, *129* (32), 9699–9704. https://doi.org/10.1002/ange.201705595.

(23) Huang, H.; Zhao, F.; Liu, L.; Zhang, F.; Wu, X. G.; Shi, L.; Zou, B.; Pei, Q.; Zhong, H. Emulsion Synthesis of Size-Tunable CH3NH3PbBr3 Quantum Dots: An Alternative Route toward Efficient Light-Emitting Diodes. *ACS Appl Mater Interfaces* **2015**, *7* (51), 28128–28133. https://doi.org/10.1021/acsami.5b10373.

(24) Li, Y.; Huang, H.; Xiong, Y.; Kershaw, S. v.; Rogach, A. L. Revealing the Formation Mechanism of CsPbBr3 Perovskite Nanocrystals Produced via a Slowed-Down Microwave-Assisted Synthesis. *Angewandte Chemie - International Edition* **2018**, *57* (20), 5833–5837. https://doi.org/10.1002/anie.201713332.

(25) Jang, D. M.; Kim, D. H.; Park, K.; Park, J.; Lee, J. W.; Song, J. K. Ultrasound Synthesis of Lead Halide Perovskite Nanocrystals. *J Mater Chem C Mater* **2016**, *4* (45), 10625–10629. https://doi.org/10.1039/C6TC04213A.

(26) Papavassiliou, G. C.; Pagona, G.; Karousis, N.; Mousdis, G. A.; Koutselas, I.; Vassilakopoulou, A. Nanocrystalline/Microcrystalline Materials Based on Lead-Halide Units. *J Mater Chem* **2012**, *22* (17), 8271–8280. https://doi.org/10.1039/C2JM15783G.

(27) Kirakosyan, A.; Kim, J.; Lee, S. W.; Swathi, I.; Yoon, S. G.; Choi, J. Optical Properties of Colloidal CH3NH3PbBr3 Nanocrystals by Controlled Growth of Lateral Dimension. *Cryst Growth Des* **2017**, *17* (2), 794–799. https://doi.org/10.1021/acs.cgd.6b01648.

(28) Zhang, F.; Huang, S.; Wang, P.; Chen, X.; Zhao, S.; Dong, Y.; Zhong, H. Colloidal Synthesis of Air-Stable CH3NH3PbI3 Quantum Dots by Gaining Chemical Insight into the Solvent Effects. *Chemistry of Materials* **2017**, *29* (8), 3793–3799. https://doi.org/10.1021/acs.chemmater.7b01100.

(29) Zhang, F.; Zhong, H.; Chen, C.; Wu, X. G.; Hu, X.; Huang, H.; Han, J.; Zou, B.; Dong, Y. Brightly Luminescent and Color-Tunable Colloidal CH3NH3PbX3 (X = Br, I, Cl) Quantum Dots: Potential Alternatives for Display Technology. *ACS Nano* **2015**, *9* (4), 4533–4542. https://doi.org/10.1021/acsnano.5b01154.

(30) Ling, Y.; Yuan, Z.; Tian, Y.; Wang, X.; Wang, J. C.; Xin, Y.; Hanson, K.; Ma, B.; Gao, H. Bright Light-Emitting Diodes Based on Organometal Halide Perovskite Nanoplatelets. *Advanced Materials* **2016**, *28* (2), 305–311. https://doi.org/10.1002/adma.201503954.

(31) Shamsi, J.; Urban, A. S.; Imran, M.; de Trizio, L.; Manna, L. Metal Halide Perovskite Nanocrystals: Synthesis, Post-Synthesis Modifications, and Their Optical Properties. *Chem Rev* **2019**, *119* (5), 3296–3348. https://doi.org/10.1021/acs.chemrev.8b00644.

(32) Petrov, A. A.; Ordinartsev, A. A.; Fateev, S. A.; Goodilin, E. A.; Tarasov, A. B. Solubility of Hybrid Halide Perovskites in DMF and DMSO. *Molecules 2021, Vol. 26, Page 7541* **2021**, *26* (24), 7541. https://doi.org/10.3390/MOLECULES26247541.

(33) Zhang, Y.; Thomas, C. J.; Guillaussier, A.; Smilgies, D. M.; Korgel, B. A. Thermal Phase Transitions in Superlattice Assemblies of Cuboidal CH3NH3PbI3 Nanocrystals Followed by Grazing Incidence X-Ray Scattering. *Journal of Physical Chemistry C*. American Chemical Society June 20, 2019, pp 17555–17565. https://doi.org/10.1021/acs.jpcc.9b03223.

(34) Petrov, A. A.; Pellet, N.; Seo, J. Y.; Belich, N. A.; Kovalev, D. Y.; Shevelkov, A. V.; Goodilin, E. A.; Zakeeruddin, S. M.; Tarasov, A. B.; Graetzel, M. New Insight into the

Formation of Hybrid Perovskite Nanowires via Structure Directing Adducts. *Chemistry of Materials* **2017**, *29* (2), 587–594. https://doi.org/10.1021/acs.chemmater.6b03965.

(35) Gu, J.; Wu, J.; Jin, C.; Sun, X.; Yin, B.; Zhang, G. C.; Wen, B.; Gao, F. Solvent Engineering for High Conversion Yields of Layered Raw Materials into Large-Scale Freestanding Hybrid Perovskite Nanowires. *Nanoscale* **2018**, *10* (37), 17722–17729. https://doi.org/10.1039/c8nr04833a.

(36) Guo, X.; McCleese, C.; Kolodziej, C.; Samia, A. C. S.; Zhao, Y.; Burda, C. Identification and Characterization of the Intermediate Phase in Hybrid Organic-Inorganic MAPbI3 Perovskite. *Dalton Transactions* **2016**, *45* (9), 3806–3813. https://doi.org/10.1039/c5dt04420k.

(37) Petrov, A. A.; Sokolova, I. P.; Belich, N. A.; Peters, G. S.; Dorovatovskii, P. V.; Zubavichus, Y. V.; Khrustalev, V. N.; Petrov, A. V.; Grätzel, M.; Goodilin, E. A.; Tarasov, A. B. Crystal Structure of DMF-Intermediate Phases Uncovers the Link between CH3NH3PbI3 Morphology and Precursor Stoichiometry. *Journal of Physical Chemistry C* **2017**, *121* (38), 20739–20743. https://doi.org/10.1021/acs.jpcc.7b08468.

(38) Ren, Y. K.; Liu, S. D.; Duan, B.; Xu, Y. F.; Li, Z. Q.; Huang, Y.; Hu, L. H.; Zhu, J.; Dai, S. Y. Controllable Intermediates by Molecular Self-Assembly for Optimizing the Fabrication of Large-Grain Perovskite Films via One-Step Spin-Coating. *J Alloys Compd* **2017**, *705*, 205–210. https://doi.org/10.1016/j.jallcom.2017.01.035.

(39) Munir, R.; Sheikh, A. D.; Abdelsamie, M.; Hu, H.; Yu, L.; Zhao, K.; Kim, T.; Tall, O. El; Li, R.; Smilgies, D. M.; Amassian, A. Hybrid Perovskite Thin-Film Photovoltaics: In Situ Diagnostics and Importance of the Precursor Solvate Phases. *Advanced Materials* **2017**, *29* (2), 1604113. https://doi.org/10.1002/adma.201604113.

(40) Wu, J.; Shan, H.; Chen, W.; Gu, X.; Tao, P.; Song, C.; Shang, W.; Deng, T. In Situ Environmental TEM in Imaging Gas and Liquid Phase Chemical Reactions for Materials Research. *Advanced Materials* **2016**, *28* (44), 9686–9712. https://doi.org/10.1002/ADMA.201602519.

(41) Ramnarain, V.; Georges, T.; Ortiz Peña, N.; Ihiawakrim, D.; Longuinho, M.; Bulou, H.; Gervais, C.; Sanchez, C.; Azaïs, T.; Ersen, O. Monitoring of CaCO3Nanoscale Structuration through Real-Time Liquid Phase Transmission Electron Microscopy and Hyperpolarized NMR. *J Am Chem Soc* **2022**, *144* (33), 15236–15251. https://doi.org/10.1021/JACS.2C05731/SUPPL_FILE/JA2C05731_SI_007.AVI.

(42) Zhu, G. Z.; Prabhudev, S.; Yang, J.; Gabardo, C. M.; Botton, G. A.; Soleymani, L. In Situ Liquid Cell TEM Study of Morphological Evolution and Degradation of Pt-Fe Nanocatalysts during Potential Cycling. *Journal of Physical Chemistry C* **2014**, *118* (38), 22111–22119. https://doi.org/10.1021/JP506857B/SUPPL_FILE/JP506857B_SI_001.PDF.

(43) Ortiz Peña, N.; Ihiawakrim, D.; Han, M.; Lassalle-Kaiser, B.; Carenco, S.; Sanchez, C.; Laberty-Robert, C.; Portehault, D.; Ersen, O. Morphological and Structural Evolution of Co3O4 Nanoparticles Revealed by in Situ Electrochemical Transmission Electron Microscopy during Electrocatalytic Water Oxidation. *ACS Nano* **2019**, *13* (10), 11372–11381. https://doi.org/10.1021/ACSNANO.9B04745.

(44) Evans, J. E.; Jungjohann, K. L.; Browning, N. D.; Arslan, I. Controlled Growth of Nanoparticles from Solution with in Situ Liquid Transmission Electron Microscopy. *Nano Lett* **2011**, *11* (7), 2809–2813. https://doi.org/10.1021/nl201166k.

(45) Kashyap, S.; Woehl, T. J.; Liu, X.; Mallapragada, S. K.; Prozorov, T. Nucleation of Iron Oxide Nanoparticles Mediated by Mms6 Protein in Situ. *ACS Nano* **2014**, *8* (9), 9097–9106. https://doi.org/10.1021/nn502551y.

(46) Khelfa, A.; Nelayah, J.; Amara, H.; Wang, G.; Ricolleau, C.; Alloyeau, D. Quantitative In Situ Visualization of Thermal Effects on the Formation of Gold Nanocrystals in Solution. *Advanced Materials* **2021**, *33* (38), 2102514. https://doi.org/10.1002/adma.202102514.

(47) Klein-Kedem, N.; Cahen, D.; Hodes, G. Effects of Light and Electron Beam Irradiation on Halide Perovskites and Their Solar Cells. *Acc Chem Res* **2016**, *49* (2), 347–354. https://doi.org/10.1021/acs.accounts.5b00469.

(48) Yuan, H.; Debroye, E.; Janssen, K.; Naiki, H.; Steuwe, C.; Lu, G.; Moris, M.; Orgiu, E.; Uji-I, H.; de Schryver, F.; Samorì, P.; Hofkens, J.; Roeffaers, M. Degradation of Methylammonium Lead Iodide Perovskite Structures through Light and Electron Beam Driven Ion Migration. *Journal of Physical Chemistry Letters* **2016**, *7* (3), 561–566. https://doi.org/10.1021/acs.jpclett.5b02828.

(49) Li, Y.; Zhou, W.; Li, Y.; Huang, W.; Zhang, Z.; Chen, G.; Wang, H.; Wu, G. H.; Rolston, N.; Vila, R.; Chiu, W.; Cui, Y. Unravelling Degradation Mechanisms and Atomic Structure of Organic-Inorganic Halide Perovskites by Cryo-EM. *Joule* **2019**, *3* (11), 2854–2866. https://doi.org/10.1016/j.joule.2019.08.016.

(50) Duchamp, M.; Hu, H.; Lam, Y. M.; Dunin-Borkowski, R. E.; Boothroyd, C. B. STEM Electron Beam-Induced Current Measurements of Organic-Inorganic Perovskite Solar Cells. *Ultramicroscopy* **2020**, *217*. https://doi.org/10.1016/j.ultramic.2020.113047.

(51) Dang, Z.; Shamsi, J.; Akkerman, Q. A.; Imran, M.; Bertoni, G.; Brescia, R.; Manna, L. Low-Temperature Electron Beam-Induced Transformations of Cesium Lead Halide Perovskite Nanocrystals. *ACS Omega* **2017**, *2* (9), 5660–5665. https://doi.org/10.1021/acsomega.7b01009.

(52) Xiao, C.; Li, Z.; Guthrey, H.; Moseley, J.; Yang, Y.; Wozny, S.; Moutinho, H.; To, B.; Berry, J. J.; Gorman, B.; Yan, Y.; Zhu, K.; Al-Jassim, M. Mechanisms of Electron-Beam-Induced Damage in Perovskite Thin Films Revealed by Cathodoluminescence Spectroscopy. *Journal of Physical Chemistry C* **2015**, *119* (48), 26904–26911. https://doi.org/10.1021/acs.jpcc.5b09698.

(53) Dang, Z.; Shamsi, J.; Palazon, F.; Imran, M.; Akkerman, Q. A.; Park, S.; Bertoni, G.; Prato, M.; Brescia, R.; Manna, L. In Situ Transmission Electron Microscopy Study of Electron Beam-Induced Transformations in Colloidal Cesium Lead Halide Perovskite Nanocrystals. *ACS Nano* **2017**, *11* (2), 2124–2132. https://doi.org/10.1021/acsnano.6b08324.

(54) Funk, H.; Shargaieva, O.; Eljarrat, A.; Unger, E. L.; Koch, C. T.; Abou-Ras, D. In Situ TEM Monitoring of Phase-Segregation in Inorganic Mixed Halide Perovskite. *Journal of*

Physical Chemistry Letters **2020**, *11* (13), 4945–4950. https://doi.org/10.1021/acs.jpclett.0c01296.

(55) Wang, W.; Ghosh, T.; Yan, H.; Erofeev, I.; Zhang, K.; Loh, K. P.; Mirsaidov, U. The Growth Dynamics of Organic-Inorganic Metal Halide Perovskite Films. *J Am Chem Soc* **2022**, *144* (39), 17848–17856. https://doi.org/10.1021/jacs.2c06022.

(56) Qin, F.; Wang, Z.; Wang, Z. L. Anomalous Growth and Coalescence Dynamics of Hybrid Perovskite Nanoparticles Observed by Liquid-Cell Transmission Electron Microscopy. *ACS Nano* **2016**, *10* (11), 9787–9793. https://doi.org/10.1021/acsnano.6b04234.

(57) Abellan, P.; Woehl, T. J.; Parent, L. R.; Browning, N. D.; Evans, J. E.; Arslan, I. Factors Influencing Quantitative Liquid (Scanning) Transmission Electron Microscopy. *Chemical Communications* **2014**, *50* (38), 4873–4880. https://doi.org/10.1039/c3cc48479c.

(58) Hermannsdörfer, J.; Tinnemann, V.; Peckys, D. B.; de Jonge, N. The Effect of Electron Beam Irradiation in Environmental Scanning Transmission Electron Microscopy of Whole Cells in Liquid. *Microscopy and Microanalysis* **2016**, *22* (3), 656–665. https://doi.org/10.1017/S1431927616000763.

(59) Chen, S.; Gao, P. Challenges, Myths, and Opportunities of Electron Microscopy on Halide Perovskites. *Journal of Applied Physics*. American Institute of Physics Inc. July 7, 2020. https://doi.org/10.1063/5.0012310.

(60) Huang, H.; Susha, A. S.; Kershaw, S. V.; Hung, T. F.; Rogach, A. L. Control of Emission Color of High Quantum Yield CH3NH3PbBr3 Perovskite Quantum Dots by Precipitation Temperature. *Advanced Science* **2015**, *2* (9), 1500194. https://doi.org/10.1002/advs.201500194.

(61) J. Rodriguez-Carvajal. "Fullprof: A Program for Rietveld Refinement and Pattern Matching Analysis," Abstract of the Satellite Meeting on Powder Diffraction of the XV Congress of the IUCr, 1990, 127.

(62) March, A. Mathematische Theorie Der Regelung Nach Der Korngestah Bei Affiner Deformation. *Z Kristallogr Cryst Mater* **1932**, *81* (1–6), 285–297. https://doi.org/10.1524/ZKRI.1932.81.1.285.

(63) Jeon, N. J.; Noh, J. H.; Kim, Y. C.; Yang, W. S.; Ryu, S.; Seok, S. il. Solvent Engineering for High-Performance Inorganic-Organic Hybrid Perovskite Solar Cells. *Nat Mater* **2014**, *13* (9), 897–903. https://doi.org/10.1038/nmat4014.

(64) Egerton, R. F.; Li, P.; Malac, M. Radiation Damage in the TEM and SEM. In *Micron*; 2004; Vol. 35, pp 399–409. https://doi.org/10.1016/j.micron.2004.02.003.

(65) Jiang, N. Electron Beam Damage in Oxides: A Review. *Reports on Progress in Physics*. Institute of Physics Publishing December 18, 2015. https://doi.org/10.1088/0034-4885/79/1/016501.

(66) Egerton, R. F. Radiation Damage to Organic and Inorganic Specimens in the TEM. *Micron*. Elsevier Ltd April 1, 2019, pp 72–87. https://doi.org/10.1016/j.micron.2019.01.005.

(67) Schneider, N. M.; Norton, M. M.; Mendel, B. J.; Grogan, J. M.; Ross, F. M.; Bau, H. H. Electron-Water Interactions and Implications for Liquid Cell Electron Microscopy. *Journal of Physical Chemistry C* **2014**, *118* (38), 22373–22382. https://doi.org/10.1021/jp507400n.

(68) Gupta, T.; Schneider, N. M.; Park, J. H.; Steingart, D.; Ross, F. M. Spatially Dependent Dose Rate in Liquid Cell Transmission Electron Microscopy. *Nanoscale* **2018**, *10* (16), 7702–7710. https://doi.org/10.1039/c8nr01935e.

(69) Schneider, N. M. Electron Beam Effects in Liquid Cell TEM and STEM. In *Liquid Cell Electron Microscopy*; Cambridge University Press, 2016; pp 140–163. https://doi.org/10.1017/9781316337455.008.

(70) Lignos, I.; Stavrakis, S.; Nedelcu, G.; Protesescu, L.; Demello, A. J.; Kovalenko, M. v. Synthesis of Cesium Lead Halide Perovskite Nanocrystals in a Droplet-Based Microfluidic Platform: Fast Parametric Space Mapping. *Nano Lett* **2016**, *16* (3), 1869–1877. https://doi.org/10.1021/acs.nanolett.5b04981.

(71) Li, Y.; Zhao, Z.; Lin, F.; Cao, X.; Cui, X.; Wei, J. In Situ Observation of Crystallization of Methylammonium Lead Iodide Perovskite from Microdroplets. *Small* **2017**, *13* (26). https://doi.org/10.1002/smll.201604125.

(72) Zhong, Y.; Munir, R.; Li, J.; Tang, M. C.; Niazi, M. R.; Smilgies, D. M.; Zhao, K.; Amassian, A. Blade-Coated Hybrid Perovskite Solar Cells with Efficiency > 17%: An In Situ Investigation. *ACS Energy Lett* **2018**, *3* (5), 1078–1085. https://doi.org/10.1021/acsenergylett.8b00428.

(73) Tan, W. L.; Kirby, N. M.; Cheng, Y. B.; McNeill, C. R. Origin of Vertical Slab Orientation in Blade-Coated Layered Hybrid Perovskite Films Revealed with in-Situ Synchrotron X-Ray Scattering. *Nano Energy* **2021**, *83*. https://doi.org/10.1016/j.nanoen.2021.105818.

(74) Dahlman, C. J.; Decrescent, R. A.; Venkatesan, N. R.; Kennard, R. M.; Wu, G.; Everest, M. A.; Schuller, J. A.; Chabinyc, M. L. Controlling Solvate Intermediate Growth for Phase-Pure Organic Lead Iodide Ruddlesden-Popper (C4H9NH3)2(CH3NH3)n-1Pb NI3 N+1 Perovskite Thin Films. *Chemistry of Materials* **2019**, *31* (15), 5832–5844. https://doi.org/10.1021/acs.chemmater.9b01952.

(75) Kim, N. K.; Min, Y. H.; Noh, S.; Cho, E.; Jeong, G.; Joo, M.; Ahn, S. W.; Lee, J. S.; Kim, S.; Ihm, K.; Ahn, H.; Kang, Y.; Lee, H. S.; Kim, D. Investigation of Thermally Induced Degradation in CH3NH3PbI3 Perovskite Solar Cells Using In-Situ Synchrotron Radiation Analysis. *Sci Rep* **2017**, *7* (1), 4645. https://doi.org/10.1038/s41598-017-04690-w.

(76) Dey, A.; Ye, J.; De, A.; Debroye, E.; Ha, S. K.; Bladt, E.; Kshirsagar, A. S.; Wang, Z.; Yin, J.; Wang, Y.; Quan, L. N.; Yan, F.; Gao, M.; Li, X.; Shamsi, J.; Debnath, T.; Cao, M.; Scheel, M. A.; Kumar, S.; Steele, J. A.; Gerhard, M.; Chouhan, L.; Xu, K.; Wu, X. G.; Li, Y.; Zhang, Y.; Dutta, A.; Han, C.; Vincon, I.; Rogach, A. L.; Nag, A.; Samanta, A.; Korgel, B. A.; Shih, C. J.; Gamelin, D. R.; Son, D. H.; Zeng, H.; Zhong, H.; Sun, H.; Demir, H. V.; Scheblykin, I. G.; Mora-Seró, I.; Stolarczyk, J. K.; Zhang, J. Z.; Feldmann, J.; Hofkens, J.; Luther, J. M.; Pérez-Prieto, J.; Li, L.; Manna, L.; Bodnarchuk, M. I.; Kovalenko, M. v.; Roeffaers, M. B. J.; Pradhan, N.; Mohammed, O. F.; Bakr, O. M.; Yang, P.; Müller-Buschbaum, P.;

Kamat, P. v.; Bao, Q.; Zhang, Q.; Krahne, R.; Galian, R. E.; Stranks, S. D.; Bals, S.; Biju, V.; Tisdale, W. A.; Yan, Y.; Hoye, R. L. Z.; Polavarapu, L. State of the Art and Prospects for Halide Perovskite Nanocrystals. *ACS Nano*. American Chemical Society July 27, 2021, pp 10775–10981. https://doi.org/10.1021/acsnano.0c08903.

(77) Masi, S.; Gualdrón-Reyes, A. F.; Mora-Seró, I. Stabilization of Black Perovskite Phase in FAPbI3and CsPbI3. *ACS Energy Letters*. American Chemical Society June 12, 2020, pp 1974–1985. https://doi.org/10.1021/acsenergylett.0c00801.

(78) Hao, F.; Stoumpos, C. C.; Liu, Z.; Chang, R. P. H.; Kanatzidis, M. G. Controllable Perovskite Crystallization at a Gas-Solid Interface for Hole Conductor-Free Solar Cells with Steady Power Conversion Efficiency over 10%. *J Am Chem Soc* **2014**, *136* (46), 16411–16419. https://doi.org/10.1021/ja509245x.

(79) Dualeh, A.; Tétreault, N.; Moehl, T.; Gao, P.; Nazeeruddin, M. K.; Grätzel, M. Effect of Annealing Temperature on Film Morphology of Organic-Inorganic Hybrid Pervoskite Solid-State Solar Cells. *Adv Funct Mater* **2014**, *24* (21), 3250–3258. https://doi.org/10.1002/adfm.201304022.

(80) Lee, J. W.; Seol, D. J.; Cho, A. N.; Park, N. G. High-Efficiency Perovskite Solar Cells Based on the Black Polymorph of HC(NH2)2PbI3. *Advanced Materials* **2014**, *26* (29), 4991–4998. https://doi.org/10.1002/adma.201401137.

(81) Rong, Y.; Tang, Z.; Zhao, Y.; Zhong, X.; Venkatesan, S.; Graham, H.; Patton, M.; Jing, Y.; Guloy, A. M.; Yao, Y. Solvent Engineering towards Controlled Grain Growth in Perovskite Planar Heterojunction Solar Cells. *Nanoscale* **2015**, *7* (24), 10595–10599. https://doi.org/10.1039/c5nr02866c.

(82) Matsui, T.; Seo, J. Y.; Saliba, M.; Zakeeruddin, S. M.; Grätzel, M. Room-Temperature Formation of Highly Crystalline Multication Perovskites for Efficient, Low-Cost Solar Cells. *Advanced Materials* **2017**, *29* (15), 1606258. https://doi.org/10.1002/adma.201606258.

(83) Liu, X. D.; Wang, Q.; Cheng, Z. Q.; Qiu, Y. H.; Zhou, L.; Wang, Q. Q. Solution-Phase Growth of Organolead Halide Perovskite Nanowires and Nanoplates Assisted by Long-Chain Alkylammonium and Solvent Polarity. *Mater Lett* **2017**, *206*, 75–79. https://doi.org/10.1016/j.matlet.2017.06.113.

(84) Kim, H. S.; Lee, C. R.; Im, J. H.; Lee, K. B.; Moehl, T.; Marchioro, A.; Moon, S. J.; Humphry-Baker, R.; Yum, J. H.; Moser, J. E.; Grätzel, M.; Park, N. G. Lead Iodide Perovskite Sensitized All-Solid-State Submicron Thin Film Mesoscopic Solar Cell with Efficiency Exceeding 9%. *Sci Rep* **2012**, *2*. https://doi.org/10.1038/srep00591.

(85) Stoumpos, C. C.; Malliakas, C. D.; Kanatzidis, M. G. Semiconducting Tin and Lead Iodide Perovskites with Organic Cations: Phase Transitions, High Mobilities, and near-Infrared Photoluminescent Properties. *Inorg Chem* **2013**, *52* (15), 9019–9038. https://doi.org/10.1021/ic401215x.

(86) Dualeh, A.; Gao, P.; Seok, S. il; Nazeeruddin, M. K.; Grätzel, M. Thermal Behavior of Methylammonium Lead-Trihalide Perovskite Photovoltaic Light Harvesters. *Chemistry of Materials* **2014**, *26* (21), 6160–6164. https://doi.org/10.1021/cm502468k.

(87) Deng, Y. H. Common Phase and Structure Misidentifications in High-Resolution Tem Characterization of Perovskite Materials. *Condens Matter* **2021**, *6* (1), 1–8. https://doi.org/10.3390/condmat6010001.

(88) Deng, Y. H.; Nest, L. G. Analysis of Misidentifications in TEM Characterisation of Organic-Inorganic Hybrid Perovskite Material. *Journal of Microscopy*. John Wiley and Sons Inc June 1, 2021, pp 195–204. https://doi.org/10.1111/jmi.13000.

(89) Park, N. G. Perovskite Solar Cells: An Emerging Photovoltaic Technology. *Materials Today* **2015**, *18* (2), 65–72. https://doi.org/10.1016/J.MATTOD.2014.07.007.

Table of Contents (TOC) Graphic